Supplement of Atmos. Meas. Tech., 8, 1685–1699, 2015
http://www.atmos-meas-tech.net/8/1685/2015/
doi:10.5194/amt-8-1685-2015-supplement

Atmospheric Measurement Techniques
Open Access

Supplement of

Improved spectral fitting of nitrogen dioxide from OMI in the 405–465 nm window

J. H. G. M. van Geffen et al.

Correspondence to: J. H. G. M. van Geffen (geffen@knmi.nl)

S1 DOAS retrieval of NO_2 slant column densities

The DOAS procedure minimises the difference between the measured spectrum $R_{\text{meas}}(\lambda)$ and a modelled spectrum $R_{\text{mod}}(\lambda)$ within a given wavelength window, in the form of minimisation of a chi-squared merit function:

$$\chi^2 = \sum_{i=1}^{N_\lambda} \left(\frac{R_{\text{meas}}(\lambda_i) - R_{\text{mod}}(\lambda_i)}{\Delta R_{\text{meas}}(\lambda_i)} \right)^2 , \tag{S1}$$

with N_λ the number of wavelengths in the fit window and $\Delta R_{\text{meas}}(\lambda_i)$ the precision of the measurements.

The measured reflectance $R_{\text{meas}}(\lambda)$ is given by:

$$R_{\text{meas}}(\lambda) = \frac{\pi\, I(\lambda)}{\mu_0\, I_0(\lambda)} , \tag{S2}$$

with $I(\lambda)$ the radiance at top-of-atmosphere, $I_0(\lambda)$ the extraterrestrial solar irradiance spectrum, and with $\mu_0 = \cos(\theta_0)$ the cosine of the solar zenith angle (the viewing geometry dependence of I is omitted for brevity). Here $I(\lambda)$ and $I_0(\lambda)$ share the same wavelength grid, i.e. an appropriate wavelength calibration has been applied prior to the DOAS fit (see Sect. 4.2 in the main paper). The $I_0(\lambda)$ in use for the DOAS retrieval of OMNO2A is an average of the solar spectra measured by OMI using the Quartz Volume Diffusor in 2005, which is used on a daily basis.

In the OMI slant column retrieval the modelled reflectance is expressed in terms of intensities, which leads to a non-linear fit problem. This approach allows to describe the effects of inelastic scattering after a scattering event has occured (as given by Eq. (1) in the main paper):

$$R_{\text{mod}}(\lambda) = P(\lambda) \cdot \exp\left[- \sum_{k=1}^{N_k} \sigma_k(\lambda) \cdot N_{\text{s},k} \right] \cdot \left(1 + C_{\text{Ring}} \frac{I_{\text{Ring}}(\lambda)}{I_0(\lambda)} \right) , \tag{S3}$$

with $P(\lambda)$ a polynomial of degree N_p, $\sigma_k(\lambda)$ the cross section and $N_{\text{s},k}$ the slant column amount of molecule k taken into account in the fit (NO_2, O_3, etc.), C_{Ring} the Ring fitting coefficient and $I_{\text{Ring}}(\lambda)/I_0(\lambda)$ the sun-normalised synthetic Ring spectrum. The Ring spectrum describes the differential spectral signatures arising from inelastic Raman scattering of incoming sunlight by N_2 and O_2 molecules. The last term between brackets in Eq. (S3) describes both the contribution of the direct differential absorption (i.e. the 1), and the modification of these differential structures by inelastic scattering (the $+C_{\text{Ring}}\, I_{\text{Ring}}(\lambda)/I_0(\lambda)$ term) to the reflectance spectrum.

An alternative approach used by most DOAS applications – including the QDOAS software (Danckaert et al., 2012) used by BIRA-IASB for the processing of data from GOME-2 and SCIAMACHY (cf. Sect. S2.1) – applies a fitting in terms of the optical density, i.e. the logarithm of the reflectance. This allows for a linearisation of the problem, by writing the modelled reflectance as follows:

$$\ln\left[R_{\text{mod}}(\lambda)\right] = P^*(\lambda) - \sum_{k=1}^{N_k} \sigma_k(\lambda) \cdot N_{\text{s},k} - \sigma_{\text{Ring}}(\lambda) \cdot C^*_{\text{Ring}} , \tag{S4}$$

with $\sigma_{\text{Ring}}(\lambda)$ the differential (pseudo-absorption) spectrum of the Ring effect and C^*_{Ring} its fitting coefficient, where $\sigma_{\text{Ring}}(\lambda)$ is constructed from the Ring radiance spectrum $I_{\text{Ring}}(\lambda)$, a reference solar spectrum $I_{\text{ref}}(\lambda)$ (which is different from the measured solar spectrum $I_0(\lambda)$ in Eq. (S3)) and a low order polynomial. DOAS applications using Eq. (S4) often also fit a non-linear offset parameter to account of atmospheric and/or instrumental stray light or residual dark current signals; such an offset parameter is not needed in the non-linear approach of Eq. (S3), because in that case the offsets are captured by the polynomial. Note that in the linear DOAS approach of Eq. (S4) the treatment of the measurement errors in the spectrum, and therewith the details of the NO_2 slant column error, is different from the non-linear approach of Eq. (S3).

QDOAS also has the option to apply a non-linear intensity fitting method instead of the linear optical density fitting method of Eq. (S4), similar to the OMNO2A non-linear fitting method of Eq. (S3), but with the Ring effect treated as a pseudo-absorber:

$$R_{\text{mod}}(\lambda) = P(\lambda) \cdot \exp\left[- \sum_{k=1}^{N_k} \sigma_k(\lambda) \cdot N_{\text{s},k} - \sigma_{\text{Ring}}(\lambda) \cdot C^*_{\text{Ring}} \right] . \tag{S5}$$

A measure of the goodness of the fit is the so-called root-mean-square (RMS) error, which is defined as follows in case of the intensity fitting approach:

$$\text{RMS} = \sqrt{\frac{1}{N_\lambda} \sum_{i=1}^{N_\lambda} \left(R_{\text{meas}}(\lambda_i) - R_{\text{mod}}(\lambda_i) \right)^2} , \tag{S6}$$

while in the linear fitting mode of QDOAS the definition is:

$$\text{RMS}^* = \sqrt{\frac{1}{N_\lambda} \sum_{i=1}^{N_\lambda} \left(\ln[R_{\text{meas}}(\lambda_i)] - \ln[R_{\text{mod}}(\lambda_i)] \right)^2} , \tag{S7}$$

which is always larger than the RMS of Eq. (S6) for the spectra investigated here. The difference between the measured and modelled reflectances is usually referred to as the residual of the slant column fit:

$$R_{\text{resid}}(\lambda) = R_{\text{meas}}(\lambda) - R_{\text{mod}}(\lambda) . \tag{S8}$$

S2 Comparison with ground-based NO_2 data

S2.1 Ground-based NO_2 observations in UV-Vis and IR

Satellite observations of NO_2 have been compared to ground-based measurements in several studies. Hendrick et al.

(2012), for example, performed an extensive comparison of measurements acquired at the Jungfraujoch station (46.5° N, 8.0° E), part of NDACC (Network for the Detection of Atmospheric Composition Change), with data from GOME-2 and SCIAMACHY. The Jungfraujoch station is located at 3580 m a.s.l., which means that most of the year the observatory is above the boundary layer and the instruments measure NO_2 in the free troposphere and stratosphere. Hendrick et al. (2012) found that the data of independent SAOZ and FTIR measurements match each other and stratospheric NO_2 data from GOME-2 and SCIAMACHY quite well (with SAOZ biased by $+8\%$ w.r.t. FTIR).

The SAOZ instrument, operated by BIRA-IASB, is a broad-band (300–600 nm) spectrometer that measures zenith scattered sunlight (Pommereau end Goutail, 1988). Vertical column densities are derived by using the standard four-step approach (e.g. Hendrick et al., 2012), using the NDACC UV/Vis Working Group recommendations. Since these are described in detail on the NDACC website[1], only the main features are given here. The NO_2 is retrieved in the 425–495 nm wavelength window, taking into account absorption by NO_2, ozone, water vapour and O_2–O_2, the Ring effect, and a 3rd order polynomial. In the conversion of slant to vertical NO_2 columns, the NDACC NO_2 AMF climatology based on the harmonic climatology of stratospheric NO_2 profile developed by Lambert et al. (1999, 2000) has been used. SAOZ measurements contaminated by strong pollution events coming from the valley below the station have been filtered out.

Using the BIRA-IASB stacked box photochemical model PSCBOX (Hendrick et al., 2004), daily initialized with SLIMCAT chemical and meteorological fields, a photochemical correction is determined: for each day, 90° solar zenith angle (SZA) sunrise and sunset SAOZ data are converted to the satellite overpass SZA of that day, after which the average of both SAOZ NO_2 column values can be compared to the corresponding satellite measurement.

The FTIR instrument, operated by the University of Liège, is a spectrometer that measures high-resolution solar absorption spectra under clear-sky conditions (Zander et al., 2008). The NO_2 retrieval is extensively described by Hendrick et al. (2012). In brief, two microwindows are used: 2914.6–2914.7 cm^{-1} and 2915.0–2915.11 cm^{-1}, taking into account absorption by ozone, water vapour and methane. Vertical profiles and corresponding column densities are derived using the Optimal Estimation-based SFIT-2 algorithm (e.g. Rinsland et al., 1998). Here also, a photochemical correction determined with the PSCBOX model is applied to the column data: for each day where FTIR measurements are available, all retrieved FTIR vertical columns are photochemically converted to the satellite overpass SZA of that day, after which the average of all corrected FTIR NO_2 columns of the day is compared to the corresponding satellite measurement.

[1] See on http://wwww.ndacc.org/ the UV/Vis (@BIRA) page.

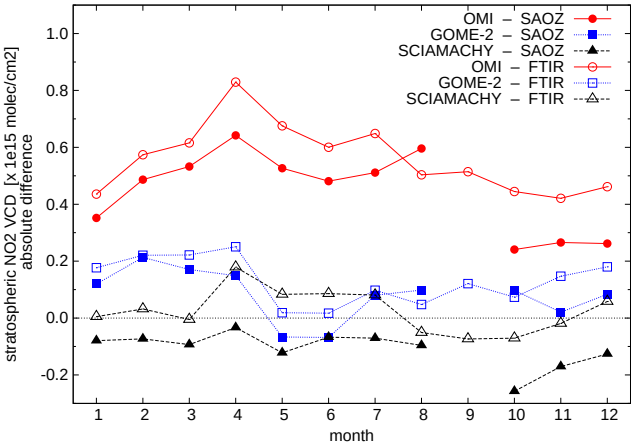

Fig. S1. Monthly average absolute differences between SAOZ (filled symbols) and FTIR (open symbols) groundbased measurements of NO_2 in 10^{15} molec/cm^2 at Jungfraujoch (46.5° N, 8.0° E) and satellite based measurements by OMI (2004–2012, red solid lines), GOME-2 (2007–2012, blue dotted lines) and SCIAMACHY (2002–2012, black dashed lines). There is insufficient SAOZ data in September for reliable averages.

Total random and systematic uncertainties on the FTIR column data have been evaluated at 11% and 36%, respectively (Hendrick et al., 2012; Table 2 in Rinsland et al., 2003). In the case of SAOZ measurements, error sources have been quoted in Van Roozendael et al. (1994) and Hendrick et al. (2012). Taking into account the past NDACC NO_2 intercomparison exercises (e.g. Vandaele et al., 2005; Roscoe et al., 2010), a total uncertainty of 12% on the retrieved NO_2 vertical columns is derived.

S2.2 Comparison with ground-based NO_2 data

The comparison of SAOZ and FTIR data at the Jungfraujoch station with satellite data by Hendrick et al. (2012) was repeated now also including OMI data and extending the GOME-2 and SCIAMACHY datasets up to the end of 2012. For this comparison the SAOZ and FTIR data have been corrected with a photochemical model (PSCBOX; Hendrick et al. (2004)) to the local overpass times of the satellite sensors. For the Jungfraujoch station the model predicts an average temporal difference between OMI and the mid-morning sensors GOME-2 and SCIAMACHY of $+0.5\times10^{15}$ molec/cm^2.

Fig. S1 shows the averaged monthly mean differences between the three satellite sensors and the SAOZ and FTIR measurements for 2007-2012. Since the data of GOME-2, SCIAMACHY, SAOZ and FTIR agree to within 0.2×10^{15} molec/cm^2, the ground-based measurements clearly suggest that OMI stratospheric NO_2 retrievals are biased high by $0.3-0.8\times10^{15}$ molec/cm^2, or $+0.5\times10^{15}$ molec/cm^2

Table S1. Average differences and corresponding standard deviations between SAOZ and FTIR groundbased measurements of NO_2 at Jungfraujoch (46.5° N, 8.0° E) and satellite based measurements by OMI, GOME-2 and SCIAMACHY, given both for the full data period and for the data period common to the satellite instruments (2007–2012). The relative difference (right column) is given as percentage of the groundbased NO_2 column values.

instruments period	absolute difference [$\times 10^{15}$ molec/cm^2]	relative difference [%]
OMI − SAOZ		
2004–2012	$+0.43 \pm 0.28$	$+18.3 \pm 12.8$
2007–2012	$+0.48 \pm 0.25$	$+20.9 \pm 12.4$
GOME-2 − SAOZ		
2007–2012	$+0.09 \pm 0.21$	$+5.4 \pm 11.2$
SCIAMACHY − SAOZ		
2002–2012	-0.12 ± 0.25	-5.2 ± 11.2
2007–2012	-0.02 ± 0.23	-1.3 ± 11.4
OMI − FTIR		
2004–2012	$+0.56 \pm 0.22$	$+23.0 \pm 11.0$
2007–2012	$+0.54 \pm 0.21$	$+21.5 \pm 9.6$
GOME-2 − FTIR		
2007–2012	$+0.12 \pm 0.17$	$+6.6 \pm 9.1$
SCIAMACHY − FTIR		
2002–2012	$+0.02 \pm 0.20$	$+0.7 \pm 9.1$
2007–2012	-0.001 ± 0.20	-0.2 ± 8.9

on average. Table S1 provides an overview of the yearly mean differences over the 2007-2012 period, as well as for the complete sensor records of SCIAMACHY (2002-2012) and OMI (2004-2012). The difference between the GOME-2 and SCIAMACHY results is of the order of 0.1×10^{15} molec/cm^2, which is consistent with the offset between GOME-2 and SCIAMACHY in stratospheric NO_2 over the Pacific Ocean.

S3 The OMI slit function & convolution of the reference spectra

The spectral resolution of the instrument covers a finite wavelength interval, which effectively averages the incident (ir)radiance – which varies on a much finer wavelength scale – over that interval: the incoming light is convolved by the so-called instrument transfer function (ITF) or slit function, with the full-width at half-maximum (FWHM) of the slit function determining the spectral resolution of the instrument. Since the reference spectra are generally measured with a much higher spectral resolution than the OMI resolution, they have to be convolved with the instrument slit function as well for usage in e.g. a DOAS retrieval. Some reference spectra are spectrally smooth (cf. Fig. S6), in which case a convolution will not make much difference. For consistency, however, all reference spectra for OMNO2A are convolved as described below.

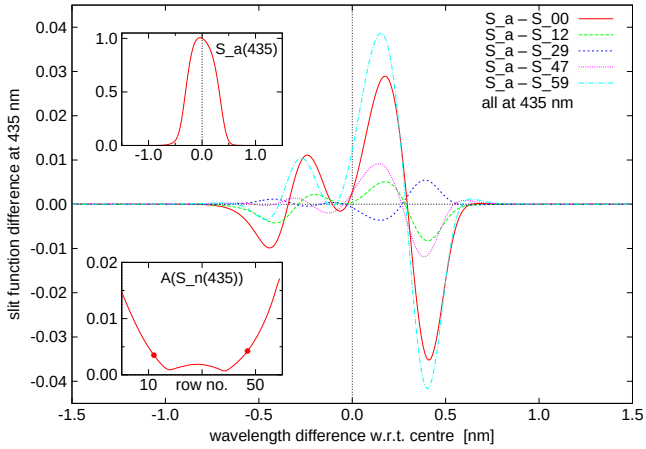

Fig. S2. *Main plot:* Difference between the OMI average slit function S_a with the slit function S_n for selected individual rows n at the centre wavelength $\lambda_i = 435$ nm. *Top inset:* The OMI average slit function at $\lambda_i = 435$ nm. *Bottom inset:* The area $A(S_n(\lambda_i))$ below the curves of the main plot as a function of the row number n, with rows 12 and 47 marked by a filled circle; see Eq. (S10) for the definition of this quantity.

S3.1 The OMI slit function

During on-ground calibrations prior to launch, the OMI slit function was measured and described by a parametrised broadened Gaussian function with a FWHM value of about 0.63 nm (Dirksen et al., 2006). The OMI slit function, designated S here, is a function of wavelength and depends on the viewing angle, i.e. it differs from detector row to detector row: $S_n(\lambda_i, \lambda)$, with $n = 0, \ldots, 59$ the row number and λ_i the wavelength of detector pixel i, which is counted along the flight track from south to north. For each λ_i the slit function covers the wavelength range $\lambda = [\lambda_i - 1.5 : \lambda_i + 1.5]$ nm, where the 1.5 nm represents approximately three times the FWHM of OMI. Within this range, the slit function is given in steps of 0.01 nm.

The operational OMNO2A processor is programmed such that it is not feasible to take the row dependency in the cross sections, i.e. in the slit function, explicitly into account. To circumvent this issue an average slit function S_a is defined for convolving the reference spectra, by taking an average over the slit functions of the middle 36 rows:

$$S_a(\lambda_i, \lambda) = \frac{1}{36} \sum_{n=12}^{47} S_n(\lambda_i, \lambda) \,, \tag{S9}$$

which is representative for most detector rows (see below). The main plot of Fig. S2 shows the difference between the average slit function and the slit functions of selected rows

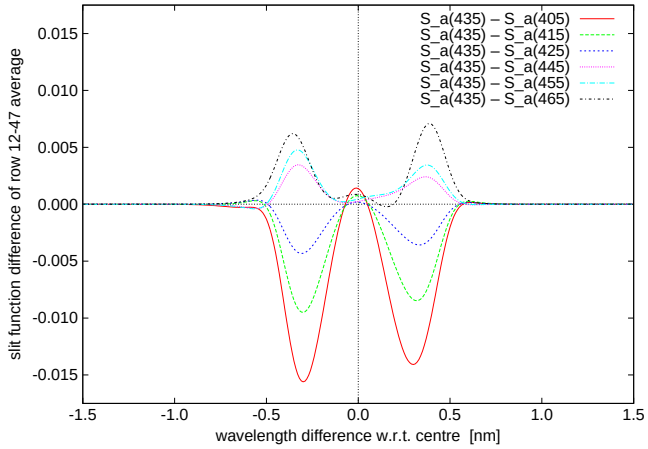

Fig. S3. Difference between the OMI average slit function S_a at $\lambda_i = 435$ nm and the average slit function at selected wavelenghts in the NO_2 fit window.

for the wavelength $\lambda_i = 435$ nm: the slit functions of rows 12–47 differ by at most 1%; for the outer rows the difference w.r.t. the average is up to 4%. The top inset of Fig. S2 shows the average slit function $S_a(\lambda_i, \lambda)$ for $\lambda_i = 435$ nm. The slit function is slightly asymmetric w.r.t. the central wavelength, and this asymmetry differs from row to row, which is why the difference curves in the main plot are not symmetric.

A measure for the difference between the average slit function S_a and the slit function S_n of an individual row is the area of the difference curves shown in Fig. S2:

$$A(S_n(\lambda_i)) = \int_{\lambda_i-1.5}^{\lambda_i+1.5} \left| S_a(\lambda_i, \lambda) - S_n(\lambda_i, \lambda) \right| d\lambda \,, \tag{S10}$$

where the integral is evaluated by way of a simple summation with steps of $\Delta\lambda = 0.01$ nm. The value of this area for $\lambda_i = 435$ nm is shown in the bottom inset of Fig. S2, with the differences for rows 12 and 47 marked by a filled circle; $A(S_{12}(\lambda_i))$ and $A(S_{47}(\lambda_i))$ are about 0.004. From this graph it is clear that S_a is representative for most of the detector rows. For the outer 5 rows on either side S_a is less representative; the slit function for rows 3 and 55, for example, differs by up to 2.5% from the average, with $A(S_3(\lambda_i))$ and $A(S_{55}(\lambda_i))$ about 0.011.

The wavelength dependency of the slit function is illustrated in Fig. S3, which shows the difference of the average slit function for selected wavelengths with the average slit function at $\lambda_i = 435$ nm (which is shown in the top inset of Fig. S2); these differences are between -1.5% for 405 nm and $+0.7\%$ for 465 nm. The curves of the differences are nearly symmetric w.r.t. the central wavelength, which means that the asymmetry of the slit function does not vary much with wavelength.

S3.2 Convolution of reference spectra

Convolution of a reference spectrum $\sigma_k^h(\lambda)$ for trace gas k can be written as follows:

$$\sigma_k(\lambda_i) = \frac{1}{S_0(\lambda_i)} \int_{\lambda_i-1.5}^{\lambda_i+1.5} \sigma_k^h(\lambda)\, S_a(\lambda_i, \lambda)\, d\lambda \,, \tag{S11}$$

where the superscript h indicates it concerns a high-resolution spectrum, and $S_0(\lambda_i)$ is the normalisation factor:

$$S_0(\lambda_i) = \int_{\lambda_i-1.5}^{\lambda_i+1.5} S_a(\lambda_i, \lambda)\, d\lambda \,. \tag{S12}$$

The limited spectral resolution of typical DOAS instruments leads to an interference between the absorption cross sections of the trace gases and the Fraunhofer structures in the solar spectrum $I_0(\lambda)$, and the division in Eq. (S2) does not fully remove the Fraunhofer structures, because the division and the convolution cannot be exchanged (e.g. Platt et al., 1997). This so-called "I_0-effect" can be corrected for by including a high-resolution solar reference reference spectrum $I_{\text{ref}}^h(\lambda)$ in the convolution. In the case of weak absorbers, like those relevant in the NO_2 fit window, Eq. (S11) is then written as follows:

$$\sigma_k(\lambda_i) = \frac{1}{S_0'(\lambda_i)} \int_{\lambda_i-1.5}^{\lambda_i+1.5} \sigma_k^h(\lambda)\, I_{\text{ref}}^h(\lambda)\, S_a(\lambda_i, \lambda)\, d\lambda \,, \tag{S13}$$

with $S_0'(\lambda_i)$ the normalisation factor:

$$S_0'(\lambda_i) = \int_{\lambda_i-1.5}^{\lambda_i+1.5} I_{\text{ref}}^h(\lambda)\, S_a(\lambda_i, \lambda)\, d\lambda \,. \tag{S14}$$

For most atmospheric absorbers the I_0-effect is weak and can often be neglected, but usually it is corrected for in the reference spectra used in the NO_2 retrieval. The $I_{\text{ref}}^h(\lambda)$ spectrum used is taken from Dobber et al. (2008); see Sect. S4.1. And $I_{\text{ref}}(\lambda)$, computed following Eq. (S11), represents the convolved reference solar spectrum.

S4 Reference spectra

As mentioned in the main paper, the relevant reference spectra for OMNO2A have been recreated taking the wavelength and row dependency of the slit function into account in the form of a row-average slit function (Sect. S3). All convolved reference spectra are created at a 0.01 nm sampling. The reference spectra labelled "v2006" refer to those used in the current OMNO2A processor (used in e.g. the DOMINO v2.0 dataset), while "v2014" refers to the updated reference spectra. The relation between these labels and the official version numbering of OMNO2A is described in Sect. S5.

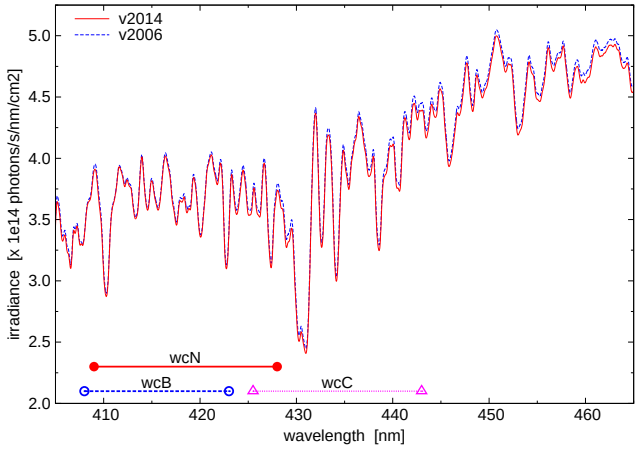

Fig. S4. Comparison of updated v2014 (solid red line) and current v2006 (dashed blue line) convolved solar reference spectrum used in OMNO2A. The two horizontal line pieces in the left bottom corner mark the old "wcB" (open circles) and new "wcN" (filled circles) window used for the wavelength calibration (Sect. 4.2 in the main paper); also shown is a test window "wcC" near the centre of the fit window.

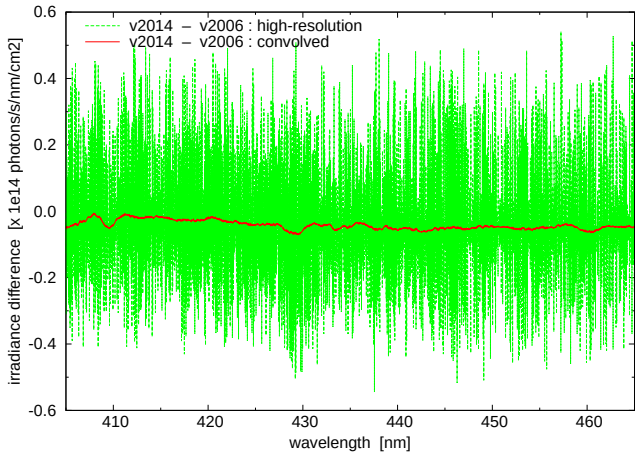

Fig. S5. Difference between the high-resolution (green dashed line) and convolved (red solid line) updated v2014 and current v2006 solar reference spectra used in OMNO2A.

S4.1 Solar reference spectrum

A high-resolution solar reference spectrum plays a key role in three aspects of the slant column processing, as it is used in: (a) the convolution of the high resolution trace gas references spectra and the generation of the H_2O_{vap} and Ring reference spectra, (b) the wavelength calibration of the Earth radiance spectrum $I(\lambda)$, and (c) the interpolation of the wavelength grid of $I(\lambda)$ onto the wavelength grid of the Solar irradiance $I_0(\lambda)$, to be able to calculate the reflectance in Eq. (S2).

The high-resolution solar reference spectrum $I^h_{\text{ref}}(\lambda)$ used for the updated OMNO2A processing is taken from Dobber et al. (2008). Fig. S4 shows a comparison of the current (v2006; see Voors et al., 2006) and updated (v2014) convolved solar reference spectra $I_{\text{ref}}(\lambda)$. Differences between the two are $1.0-1.5\%$ at most wavelengths; near 430 nm, the difference is 2.1%, while below 420 nm the differences is less than 1.0%. The absolute differences between both the high-resolution and the convolved spectra is shown in Fig. S5.

S4.2 Absorption reference spectra

This section discusses the trace gas reference spectra used in the OMI NO_2 DOAS fit – see Sect. 4.1 of the main paper. The updated (v2014) absorption reference spectra are shown in Fig. S6, while the differences between the current (v2006) and new spectra of some absorbers are shown in Fig. S7.

NO_2

The source for the NO_2 cross sections, the 220 K dataset of Vandaele et al. (1998), remains unchanged. Small differences between the current v2006 and the updated v2014 NO_2 reference spectra, seen in the top-left panel of Fig. S7, are related to the use of the updated slit function and $I^h_{\text{ref}}(\lambda)$ in the convolution given by Eq. (S13). These differences are of the order of $1-3\%$ and are therefore not expected to lead to significant changes in the retrieved NO_2 value.

O_3

The O_3 cross sections for the visible range in the current OMNO2A were based on the data from WMO (1975). These cross sections are replaced by the 223 K dataset from Bogumil et al. (2000), version 3.0 (Dec. 2004), which is resampled using a cubic spline interpolation on a 0.01 nm grid and subsequently convolved with Eq. (S13). The top-right panel of Fig. S7 shows a comparison of the v2006 and v2014 O_3 reference spectra: for most wavelengths the difference is more or less an offset; at 420 nm the difference is about 35%, at 450 nm about 10%.

H_2O_{vap}

Absorption by water vapour (H_2O_{vap}) takes place in the form of a multitude of spectrally fine absorption lines, rather than as a smooth function of wavelength, so that Eq. (S13) cannot be simply applied to create a convolved reference spectrum suitable for the DOAS retrieval. Instead, an effective reference spectrum for H_2O_{vap} absorption is determined from two simulated reflectance spectra, one with and one without water vapour absorption determined following Sneep et al. (2013):

$$R(\lambda) = R_0(\lambda)\left(1 - N_{\text{s},H_2O_{vap}} \cdot \sigma_{H_2O_{vap}}(\lambda)\right) , \qquad \text{(S15)}$$

where $R(\lambda)$ is a reflectance spectrum with a water vapour concentration with slant column value $N_{\text{s},H_2O_{vap}}$ and $R_0(\lambda)$ a reflectance spectrum without water vapour.

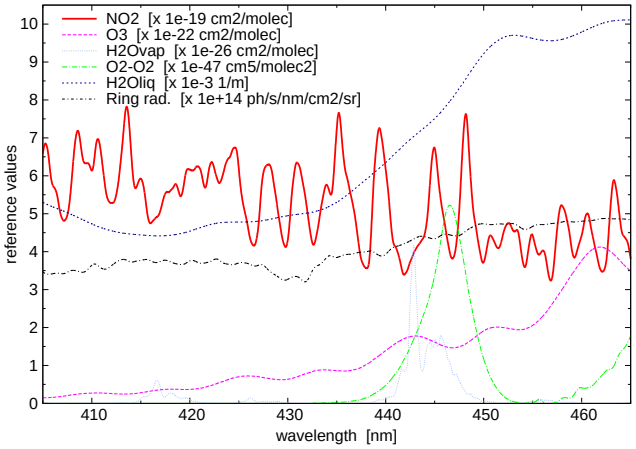

Fig. S6. Graph of the absorption spectra of NO_2, O_3, H_2O_{vap}, O_2–O_2 and H_2O_{liq}, as well as the Ring radiance spectrum (I_{Ring}) taken into account in the DOAS fit of the updated OMNO2A processor.

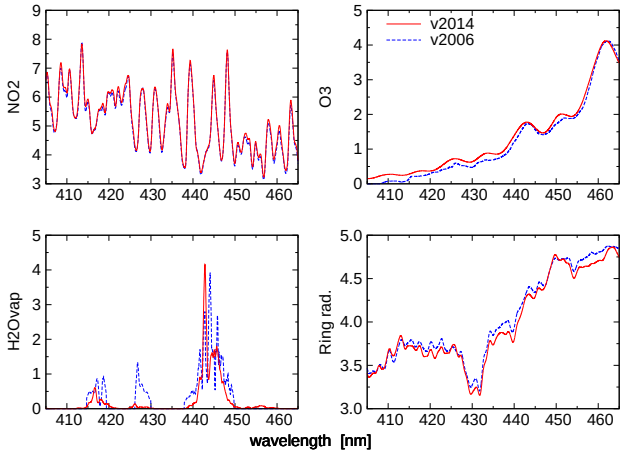

Fig. S7. Comparison of updated v2014 (solid red lines; cf. Fig. 3 in the main paper) and current v2006 (dashed blue lines) references spectra of the trace gases NO_2 (top left; $\times 10^{-19}$ cm^2/molec), O_3 (top right; $\times 10^{-22}$ cm^2/molec) and H_2O_{vap} (bottom left; $\times 10^{-26}$ cm^2/molec), and the Ring radiance spectrum (bottom right; $\times 10^{14}$ ph/s/nm/cm^2/sr) in the OMNO2A processing. Note that absorption by O_2–O_2 and H_2O_{liq} was previously not accounted for in OMNO2A.

Both $R(\lambda)$ and $R_0(\lambda)$ are simulated with the radiative transfer code DISAMAR (de Haan, 2011) in a line-by-line forward calculation on the basis of the high-resolution solar spectrum $I^h_{\text{ref}}(\lambda)$ mentioned in Sect. S4.1 and the absorption lines of all six isotopes of H_2O_{vap} from the HITRAN 2012 database (Rothman et al., 2013), without any other atmospheric trace gases present (obviously the main atmospheric gases O_2 and N_2 are present). The simulations use US standard atmosphere profiles (Anderson et al., 1986) for pressure, temperature and H_2O_{vap}, where the latter has a total column amount of 4.76×10^{22} molec/cm^2. In the simulations of $R(\lambda)$ and $R_0(\lambda)$, convolution with the OMI slit function and the I_0-correction (cf. Sect. S3.2) are automatically applied.

After simulating $R(\lambda)$ and $R_0(\lambda)$, and using that $N_{s,H_2O_{vap}} = 4.76\times10^{22}$ molec/cm^2, Eq. (S15) provides the absorption reference spectrum $\sigma_{H_2O_{vap}}(\lambda)$. Since this spectrum results from narrow line absorption features, there is no need to subtract a low-order polynomial, as is custom to generate differential absorption spectra: $\sigma_{H_2O_{vap}}(\lambda)$ is the absorption reference spectrum suitable for use in a DOAS retrieval.

The bottom-left panel of Fig. S7 compares the updated v2014 H_2O_{vap} reference spectrum and the current v2006 one, which is based on Harder and Brault (1997) and was updated in 2007 based on HITRAN 2004 data. Some absorption peak values in the ranges 440–450 nm and 415–420 nm are clearly reduced, while the absorption in the range 425–430 nm is much weaker in the v2014 reference spectrum. Note also that some of the peaks in the v2006 seem to be narrower than the OMI slit function, indicating that something was clearly wrong with the v2006 H_2O_{vap} spectrum.

O_2–O_2

The collision between two oxygen molecules in the atmosphere gives rise to so-called O_2–O_2 absorption. The absorption peak around 446 nm lies in the NO_2 fit window, as does the tail of the absorption peak around 477 nm (cf. Fig. S6). The latter peak is used in the OMI OMCLDO2 data product for the retrieval of cloud information within the 460–490 nm wavelength window.

In the current OMNO2A processing, absorption by O_2–O_2 was not taken into account, as tests with v2006 pointed out that including O_2–O_2 did not significantly affect the RMS error of the fit (cf. Bucsela et al., 2006). As described in Sect. 5.2 in the main paper, however, including O_2–O_2 improves the NO_2 fit in other ways.

Recently Thalman and Volkamer (2013) have released a new cross section database for O_2–O_2 absorption, given at 293 K and 203 K, which compares very well with the data from Hermans et al. (1999) – which is used in many NO_2 retrievals, such as for the GOME-2 and SCIAMACHY data used above, and also for the OMCLDO2 cloud product – but has a higher signal-to-noise. For this reason the Thalman and Volkamer (2013) 293 K cross section data are selected as v2014 reference spectrum, but with a correction for a small spurious jump around 432 nm, for which the 203 K spectrum is used. Subsequently, the spectrum is resampled using a cubic spline interpolation on a 0.01 nm grid, followed by a convolution with Eq. (S13).

H_2O_{liq}

Accounting for absorption of light by liquid water (H_2O_{liq}), in particular in clear ocean water, has been considered before in the retrieval of glyoxal (Lerot et al., 2010) and of NO_2 (Richter et al., 2011). In the current OMNO2A processing H_2O_{liq} is not taken into account. As described in Sect. 5.2 of the main paper including H_2O_{liq} clearly improves the spectral fit of NO_2 for clear-sky situations over clear ocean waters when using a fit window that is wider than 425–450 nm.

The absorption coefficients of liquid water are taken from Table 3 of Pope and Fry (1997). This reference spectrum is very smooth with wavelength, as can be seen in Fig. S6, so that a convolution of the spectrum is not strictly necessary. For consistency, however, convolution and I_0-correction are applied as with the other reference spectra. The absorption coefficients $\sigma_{H_2O_{liq}}$ have unit m^{-1}, so that the fit coefficient $N_{s,H_2O_{liq}}$ is the length of the average light path in water (in m).

Ring effect

Accounting for the Ring effect (Grainger and Ring, 1962; Chance and Spurr, 1997) in the spectral fit requires either a Ring radiance spectrum $I_{Ring}(\lambda)$ or a (pseudo) Ring differential cross section $\sigma_{Ring}(\lambda)$, where the latter is essentially the difference between I_{Ring} divided by a reference solar spectrum and subtracting a low order polynomial.

For OMNO2A the $I_{Ring}(\lambda)$ is computed following Chance and Spurr (1997), using the updated slit function, with the radiative transfer code DISAMAR (de Haan, 2011) in a line-by-line forward calculation on the basis of the high-resolution solar spectrum $I^h_{ref}(\lambda)$, assuming a pure Rayleigh atmosphere, i.e. without absorbing trace gases. The bottom-right panel of Fig. S7 shows the current v2006 and the updated v2014 Ring radiance reference spectra $I_{Ring}(\lambda)$ for the non-linear OMNO2A retrieval; differences are of the order of 2%. The $\sigma_{Ring}(\lambda)$ for the linear tests in Sect. 5.3 in the main paper is constructed by subtracting a 2nd order polynomial from the ratio $I_{Ring}(\lambda)/I_{ref}(\lambda)$.

S4.3 Ring coefficient and detector row 0

In the current v2006 OMNO2A processing, the term for the Ring effect contains a normalisation factor, which ensures that the ratio $I_{Ring}(\lambda)/I_0(\lambda)$ in Eq. (S3) is about 1 (one) for the fit window. This normalisation clearly affects the resulting value of the C_{Ring} fit coefficient. In the new v2014 OMNO2A processing, the Ring normalisation option is switched off, thus giving more physically meaningful results for the coefficient C_{Ring}.

The OMI solar irradiance $I_0(\lambda)$ used in the DOAS retrieval (see Sect. S1) is given as one spectrum for each of the 60 detector rows: $I_0(\lambda, n)$, with $n = 0, 1, \ldots, 59$ the row number, where row 0 (59) is at the western (eastern) most end of the swath. Since observing the sun is essentially viewing angle independent, one expects that the $I_0(\lambda, n)$ measured by OMI is essentially the same for the 60 detector rows (any difference being related only to the row and wavelength dependency of the OMI slit function).

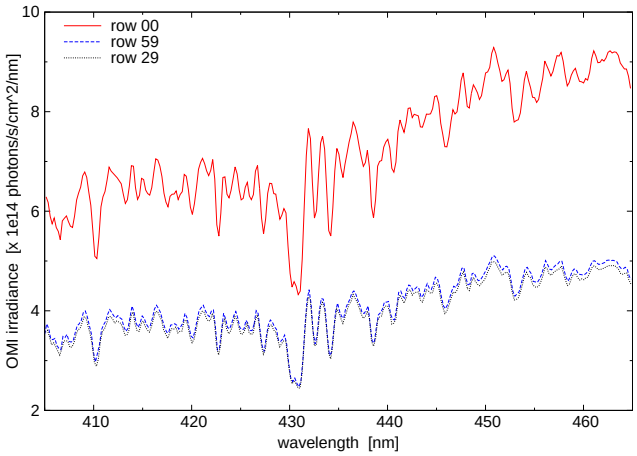

Fig. S8. OMI solar irradiance spectra in the NO_2 fit window for three detector row pixels: row 0 (red solid line), row 59 (blue dashed line), and row 29 as example for the intermediate rows (magenta dotted line). The irradiance spectra for rows 1 through 58 are indistinguishable from one another when plotted in this manner; any small difference between them is related only to the row and wavelength dependency of the OMI slit function.

But the $I_0(\lambda, 0)$ appears to be much higher and the $I_0(\lambda, 59)$ a little higher than the irradiance for rows 1 through 58. This is illustrated in Fig. S8, which uses the irradiance of row 29 as being representative for rows 1 through 58. To bring the irradiance of the outer two rows to the irradiance level of the other rows, $I_0(\lambda, 0)$ needs to be multiplied by 0.55 and $I_0(\lambda, 59)$ by 0.98.

The reason that $I_0(\lambda, 0)$ and $I_0(\lambda, 59)$ are higher than the irradiance of the other rows lies in the fact that the outer two ground pixels are not correctly matched onto the detector and the level 0-to-1b processor does not account for this when scaling the irradiance (Q. Kleipool, pers. comm.). For the same reason, also the Earth radiances $I(\lambda, n)$ (not shown) for rows 0 and 59 are too high by the same factor.

As a result, the reflectance given by Eq. (S2) is not affected and the problem of too high (ir)radiance values for rows 0 and 59 does not show up in the fit parameters directly linked to the reflectance, i.e. the coefficients of the polynomial, the trace gas slant columns in Eq. (S3) and Eq. (S4), and the Ring coefficient in the linear fit approach of Eq. (S4), nor in the errors on these fit parameters. It will, however, show up in the Ring term of the OMNO2A non-linear fit approach of Eq. (S3), because of the division by $I_0(\lambda)$, now that the normalisation of $I_{Ring}(\lambda)/I_0(\lambda)$ mentioned at the beginning of this section has been switched off.

This is illustrated Fig. S9, which shows the Ring fit coefficient as a function of the detector row number for the cur-

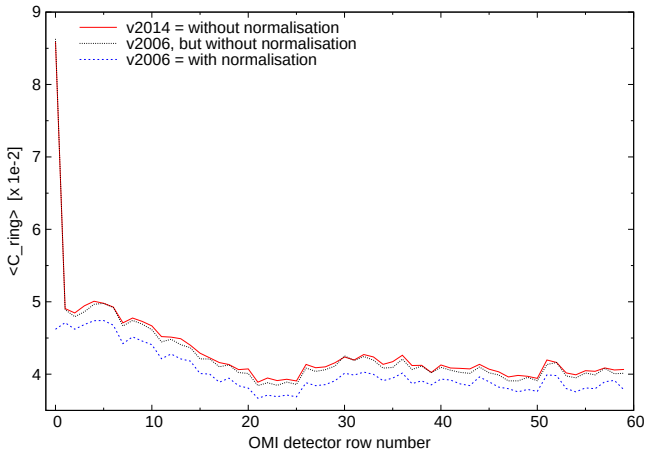

Fig. S9. Average Ring coefficient from the OMNO2A non-linear fit as a function of the OMI detector row number, for three cases: the current v2006 data (dashed blue line), the v2006 settings but with the normalisation switched off (dotted black line), and the updated v2014 data (solid red line); the difference between the latter two is caused by the updates described in the main paper. The average is computed over the 863 along track pixels of the swaths with their row-0 ground pixels in the latitude range $[-50 : +50]$ of the Pacific Ocean test orbit.

rent v2006 processing with Ring normalisation (dashed blue line), the same settings but with the normalisation switched off (dotted black line) and the updated v2014 processing for which the normalisation is switched off (solid blue line). The Ring coefficient of row 0 is clearly much higher when normalisation is switched off, and the other updates of the processing described in the main paper have little effect on the Ring coefficient. Multiplying the v2014 Ring coefficient of row 0 by the above mentioned factor of 0.55 brings its value to 0.0473, which is close to the v2006 row 0 value, somewhat low compared to the v2014 values for rows 1 and above, but all in all a reasonable value. At row 59 the irradiance is only marginally higher than it should be, which is not visible in the Ring coefficient.

S5 OMNO2A processor version numbering

The OMI NO_2 slant column retrieval processor OMNO2A provides the data in HDF-EOS files. These files are input for the processors that provide NO_2 vertical stratospheric and tropospheric column data, notably the DOMINO datasets from KNMI and NASA's "Standart Product" (SP). The OMNO2A data files are given a version number consisting of three or four digits, where the 4th digit refers to minor bug fixes only and is ignored here.

Table S2 lists the changes in the OMNO2A versions relevant in view of the updates described in this paper. The first column gives the main version number, the second the date this version was introduced. The data range covered by the version is given in the third column, but only for the versions of which the NO_2 SCD data is in use for subsequent processing, which is listed in the last column of the Table. The version of the reference spectra (Sect. 4.1) is given in the fourth column and the version of the wavelength calibration (Sect. 4.2) in the fifth column.

The current OMNO2A processor runs in two branches, each with its own version number: 1.1.1 for the DOMINO v2.0 NO_2 data products and 1.2.3 for the NASA SP v2.1 NO_2 data products. The differences between these two lies mainly in the update of the surface albedo and cloud cover data transferred to the NO_2 SCD data files as well as a number of additional HDF-EOS attributes for tracking data pixel quality; these differences do not affect the NO_2 SCD data itself. The version number "v1" used in Sect. 5, refers to these NO_2 SCD data, i.e. to the data of OMNO2A versions 1.0.5 – 1.2.3, while the version number "v2" refers to the forthcoming data with OMNO2A version 2.0.

For the forthcoming TROPOMI NO_2 processing it is planned to provide more information regarding the versions of the different processing elements in the meta data of the final NO_2 data product.

S6 Comparison between OMNO2A and QDOAS

As noted in Sect. 5.3 of the main paper, the NO_2 SCD differences displayed in Fig. 11 show a clear latitudinal variation around latitudes $20°$ S and $20°$ N – areas of the Pacific Ocean where absorption in liquid water plays a role (cf. Sect. 5.2) – for the three curves where QDOAS was used in the linear fitting mode, while for QDOAS's non-linear fitting mode the differences with OMNO2A are nearly independent of latitude. This may indicate that the linear fitting method deals differently with the polynomial-like signature of H_2O_{liq} and/or O_3 and/or O_2–O_2 absorption (cf. Fig. S6) than the non-linear fitting method, possibly due to interference of the reference spectra with the DOAS polynomial.

A detailed investigation of this issue is beyond the scope of this paper, but a clue for the origin of it is visible in Fig. S10, which shows the differences of the SCDs of NO_2, O_3 and O_2–O_2 and the fit coefficient of H_2O_{liq} between the new v2 OMNO2A results and results obtained with QDOAS in the linear (filled symbols) and non-linear (open symbols) fitting approach for the standard OMI fit window 405–465 nm. The differences are given in arbitrary units which are constructed as follows. From each difference "OMNO2A – QDOAS" the average value is subtracted to ensure the difference lies around zero. The differences for the QDOAS linear fitting approach (filled symbols) are then scaled such that the maximum values near latitude $20°$ S are around one (but not exactly one, to make sure the curves do not overlap fully). The same scaling is also applied to the curves for the QDOAS

Table S2. Numbering of the NO_2 slant column retrieval processor OMNO2A versions relevant for the updates described in this paper. See Sect. S5 for details on the columns.

version number	introduced	data range	reference spectra	wavel. calib.	description	used in
1.0.0	12 Aug. 2006	—	v2006	wcA	updated reference spectra introduced	—
1.0.5	19 July 2007	01 Oct. 2004 10 Feb. 2009	v2006	wcA	bug fixes	DOMINO v2.0
1.1.0	21 Jan. 2009	11 Feb. 2009 26 Feb. 2009	v2006	wcB	OMNO2A's wavelength calibration introduced	DOMINO v2.0
1.1.1	26 Feb. 2009	27 Feb. 2009 present	v2006	wcB	OMNO2A's wavelength calibration improved	DOMINO v2.0
1.2.0	19 Apr. 2010	—	v2006	wcB	switch from 3 to 5-yr OMI surface albedo database	—
1.2.2	16 Mar. 2011	—	v2006	wcB	switch to updated cloud product OMCLDO2 v1.2.2	—
1.2.3	24 May 2011	01 Oct. 2004 present	v2006	wcB	bug fixes	NASA SP v2.1
2.0	TBD	01 Oct. 2004 present	v2014	wcN	updates described in this paper	DOMINO v3.0 NASA SP v3 ?

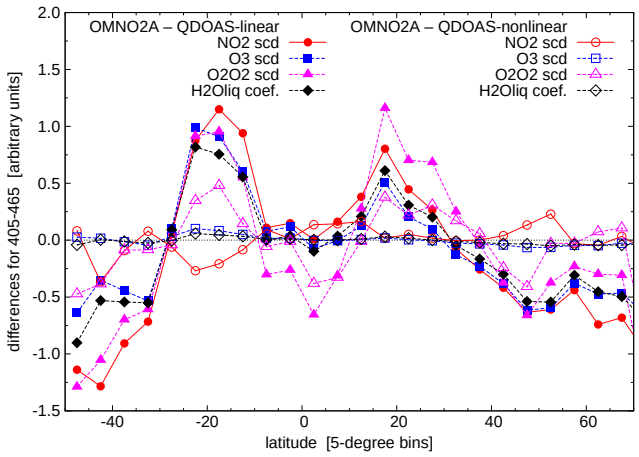

Fig. S10. Differences of the fit coefficients between the new v2 OMNO2A results and processing with QDOAS using a linear (filled symbols) and non-linear (open symbols) fitting approach in the standard OMI fit window for the Pacific Ocean test orbit. Given are the differences for NO_2 (red circles), O_3 (blue squares), O_2–O_2 (magenta triangles) and H_2O_{liq} (black diamonds) in arbitrary units, with the same scaling for both sets.

non-linear approach (open symbols), so that the differences for the two fitting approaches can be compared in magnitude.

The structure around latitudes $\pm 20°$ is clearly visible in all four SCDs for the QDOAS linear approach (filled symbols). For NO_2 (red circles) the structure is fully gone at $20°$ N and smaller and negative at $20°$ S when using the non-linear fit approach, as is also visible in Fig. 11. For both O_3 (blue squares) and H_2O_{liq} (black diamonds) the structure is fully absent when using the non-linear fit approach, while for O_2–O_2 (magenta triangles) the magnitude of the structure is about halved. For higher latitudes, both south and north, the differences are much smaller for the non-linear fitting approach in QDOAS than for the linear approach, a further indication that the two fitting approaches behave differently.

The curves for the differences in the fitting coefficients for H_2O_{vap} and the Ring effect (not shown) do not show clear latitudinal structures. For the Ring coefficient the two fitting approaches of QDOAS, Eqs. (S4) and (S5), give the same difference with OMNO2A, Eq. (S3), showing that the C^*_{Ring} in both approaches are essentially the same, while the difference between QDOAS and OMNO2A is related to the different implementation of the Ring effect in the fitting method. For the H_2O_{vap} the difference with OMNO2A is somewhat closer to zero for the non-linear than for the linear fitting approach.

S7 Reprocessed OMI NO_2 data of 2005

Sect. 5.4 in the main paper introduces the NO_2 data resulting from a reprocessing of the OMI data of 2005 with the updated OMNO2A processor. This section presents some additional material based on that data.

Per day the current (case 0) and the updated (case 4) data of the ground pixels of all OMI full swath orbits with SZA $\leq 75°$ are gridded on a $0.25° \times 0.25°$ grid. From these daily files, monthly average gridded data files are made for further analysis. To not be unnecessarily distracted by high slant column value over the polar regions, related to the viewing geometry at high latitudes, the maps shown in this section are limited to the latitude range $[-65° : +65°]$.

Similar to the maps for July 2005 in Figs. 13-14, Fig. S11 shows the monthly average gridded NO_2 slant columns of the updated (case 4) data, and the corresponding difference with the current (case 0) data, for January 2005, while the RMS

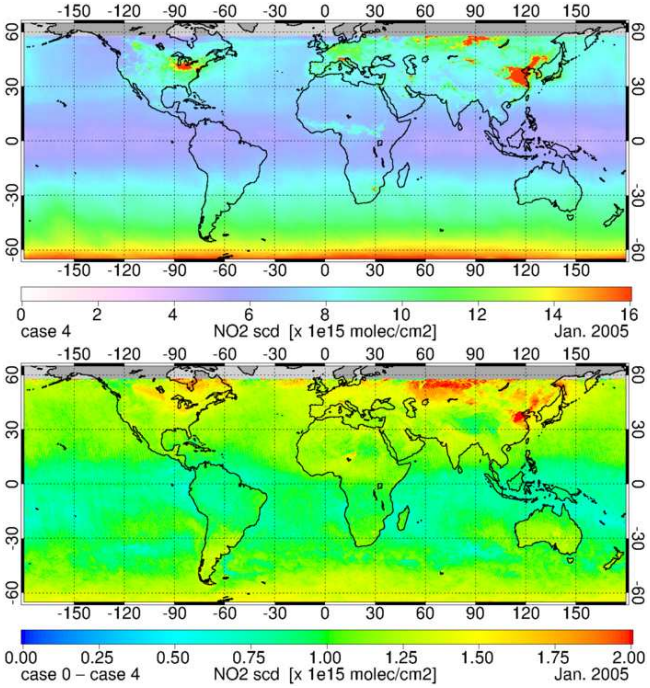

Fig. S11. Monthly average gridded updated (case 4; top panel) NO_2 slant column data for January 2005 and the corresponding difference with the current (case 0) data (lower panel).

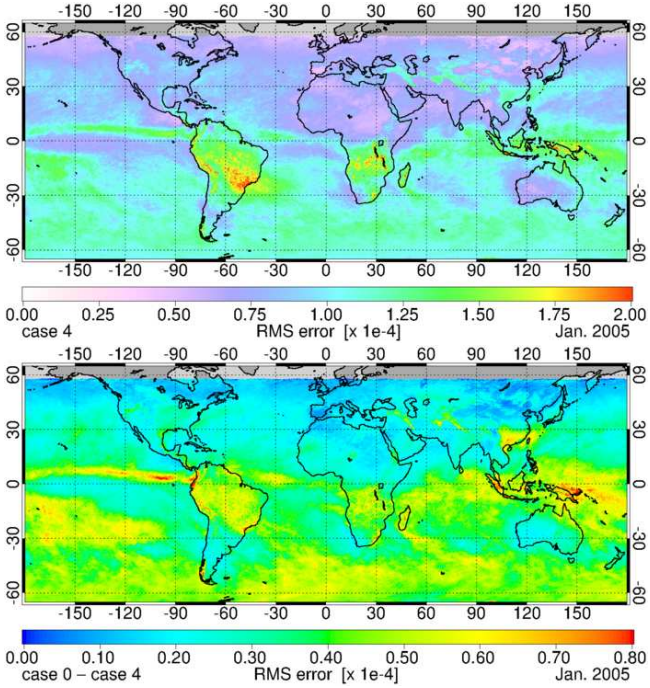

Fig. S12. Monthly average gridded updated (case 4; top panel) RMS error data for January 2005 and the corresponding difference with the current (case 0) data (lower panel).

error data for the same month is shown in Fig. S12. The map of the NO_2 difference in Fig. S11 shows a relatively large decrease in the NO_2 over China. Looking only at cloudy ground pixels (not shown), the decrease over China is not dissimilar to other areas, confirming that the tropospheric NO_2 column decreases more over polluted areas than over clean areas, as mentioned in the main paper.

Fig. S13 shows the monthly average gridded NO_2 slant column errors of the updated (case 4) data, and the corresponding difference with the current (case 0) data, for July 2005. Over the open ocean areas the NO_2 error decreases markedly, related to the improvement of the fit because of including liquid water and O_2–O_2 absorption.

Fig. 9 in the main paper shows the H_2O_{liq} fit coefficient along the OMI orbits for 1 July 2005. The monthly average H_2O_{liq} fit coefficient is shown in Fig. S14, for all ground pixel (top panel), for clear-sky pixels only (defined as pixels with cloud fraction < 0.05; middle panel) and cloudy pixels only (cloud fraction > 0.80; bottom panel). The correlation between the H_2O_{liq} fit coefficient for clear-sky pixels and the chlorophyll concentration, shown in Fig. S15, is evident. The average of the H_2O_{liq} fit coefficient plotted in Fig. S14 over all pixels is 1.26 m; while for all cloudy pixels the avearage is 0.13 m. For clear-sky pixels, the average is 0.79 m over land and 2.86 m over seas and oceans.

The areas where liquid water absorption plays a role also show up in the difference between the current (case 0) and updated (case 4) fit results for the O_3 slant column, as can be seen in Fig. S16, in agreement with what is noted in Sect. 5.2 of the main paper. To complete the presentation of the monthly average fit results for July 2005, Fig. S17 shows a map of the H_2O_{vap} slant column, Fig. S18 of the O_2–O_2 slant column, and Fig. S19 of the Ring coefficient C_{Ring}.

References

Anderson, G.P., Clough, S.A., Kneizys, F.X., Chetwynd, J.H. and Shettle, E.P.: AFGL Atmospheric Constituent Profiles, Air Force Geophys. Lab., Hanscom AFB, Mass., Tech. Rep. AFGLTR-86-0110, 1986.

Boersma, K.F., Eskes, H.J. and Brinksma, E.J.: Error analysis for tropospheric NO_2 retrieval from space, J. Geophys. Res., 109, D04311, doi:10.1029/2003JD003962, 20 pp., 2004.

Bogumil, K., Orphal, J. and Burrows, J.P.: Temperature dependent absorption cross sections of O_3, NO_2, and other atmospheric trace gases measured with the SCIAMACHY spectrometer, in *Looking down to Earth in the New Millennium*, Proceedings of the ERS-ENVISAT Symposium, 16–20 October 2000, Gothenburg, Sweden, ESA publication SP-461, 2000.

Bucsela, E.J., Celarier, E.A., Wenig, M.O., Gleason, J.F., Veefkind, J.P., Boersma, K.F. and Brinksma, E.J.: Algorithm for NO_2 vertical column retrieval from the ozone monitoring instrument, IEEE Trans. Geosci. Rem. Sens., 44, 1245-1258, doi:10.1109/TGRS.2005.863715, 2006.

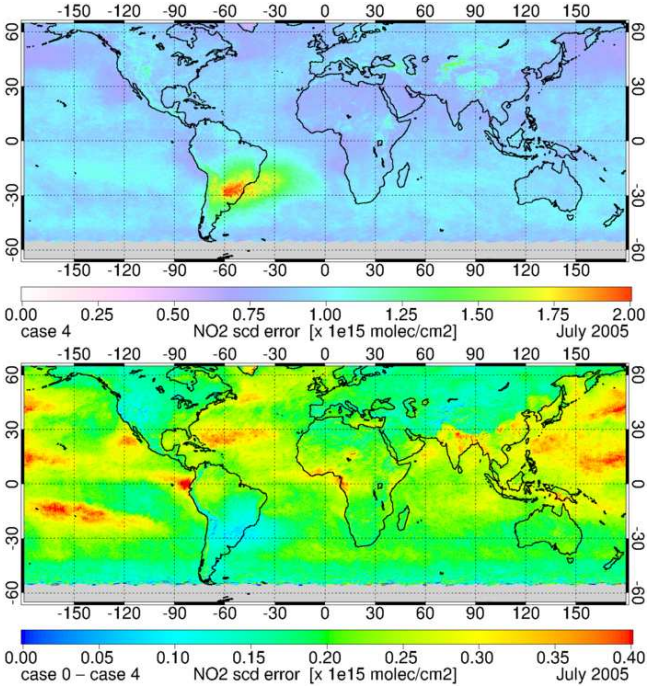

Fig. S13. Monthly average gridded updated (case 4; top panel) NO_2 slant column error data for July 2005 and the corresponding difference with the current (case 0) data (lower panel).

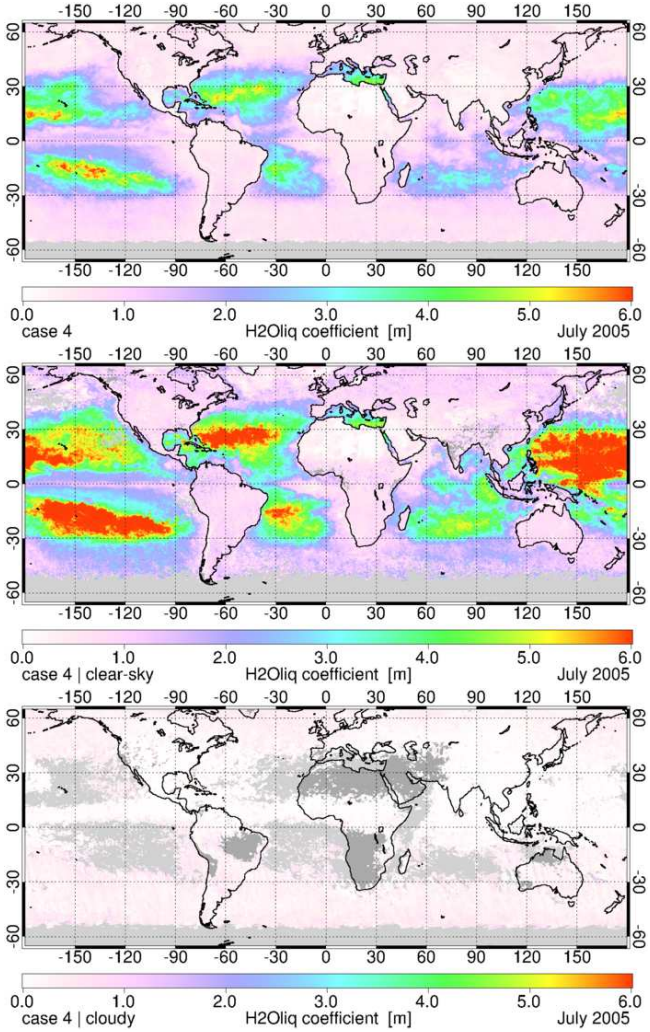

Fig. S14. Monthly average gridded H_2O_{liq} fit coefficient for July 2005 for all ground pixels (top panel), clear-sky ground pixels only (middle panel) and cloudy pixels only (bottom panel).

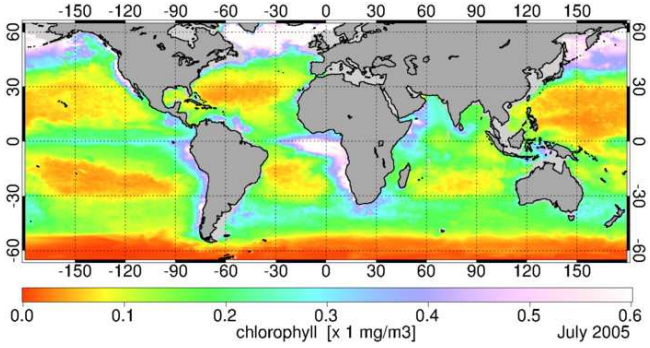

Fig. S15. Monthly average gridded chlorophyll concentration for July 2005. [Data source: NASA; cf. footnote 4 in the main paper.]

Chance, K.V. and Spurr, R.J.D.: Ring effect studies: Rayleigh scattering, including molecular parameters for rotational Raman scattering, and the Fraunhofer spectrum, Appl. Optics, 36, 21, 5224-5230, 1997.

Danckaert, T., Fayt, C. and Van Roozendael, M.: QDOAS software user manual, Version 2.1, Dec. 2012, BIRA-IASB, Brussels, Belgiun, 2012.

de Haan, J.F.: DISAMAR – Determining Instrument Specifications and Analyzing Methods for Atmospheric Retrieval – Algorithm description and background information, RP-TROPOMI-KNMI-066, issue 2.2.1, KNMI, The Netherlands, 2011.

Dirksen, R., Dobber, M.R., Voors, R. and Levelt, P.: Pre-launch characterization of the Ozone Monitoring Instrument transfer function in the spectral domain, Appl. Optics, 45, 17, 3972-3981, doi:10.1364/AO.45.003972, 2006.

Dobber, M., Voors, R., Dirksen, R., Kleipool, Q. and Levelt, P.: The high-resolution solar reference spectrum between 250 and 550 nm and its application to measurements with the Ozone Monitoring Instrument, Solar Physics, 249, 281-291, doi:10.1007/s11207-008-9187-7, 2008.

Grainger, J.F. and Ring, J.: Anomalous Fraunhofer line profiles, Nature, 193, 762, doi:10.1038/193762a0, 1962.

Harder, J.W. and Brault, J.W.: Atmospheric measurements of water vapor in the 442-nm region, J. Geophys. Res., 102, 6245-6252, doi:10.1029/96JD01730, 1997.

Hendrick, F., Barret, B., Van Roozendael, M., Boesch, H., Butz, A., De Mazière, M., Goutail, F., Hermans, C., Lambert, J.-C., Pfeilsticker, K. and Pommereau, J.-P.: Retrieval of nitrogen dioxide stratospheric profiles from ground-based zenith-

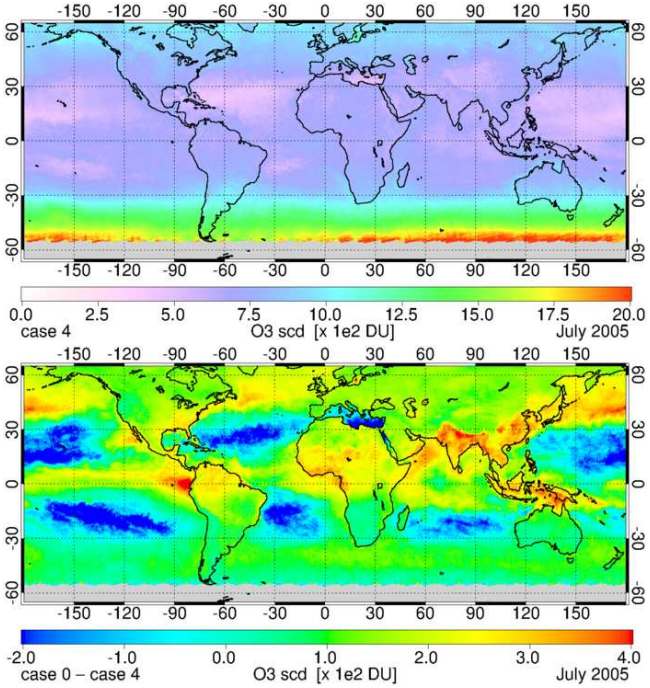

Fig. S16. Monthly average gridded updated (case 4; top panel) O_3 slant column data for July 2005 and the corresponding difference with the current (case 0) data (lower panel).

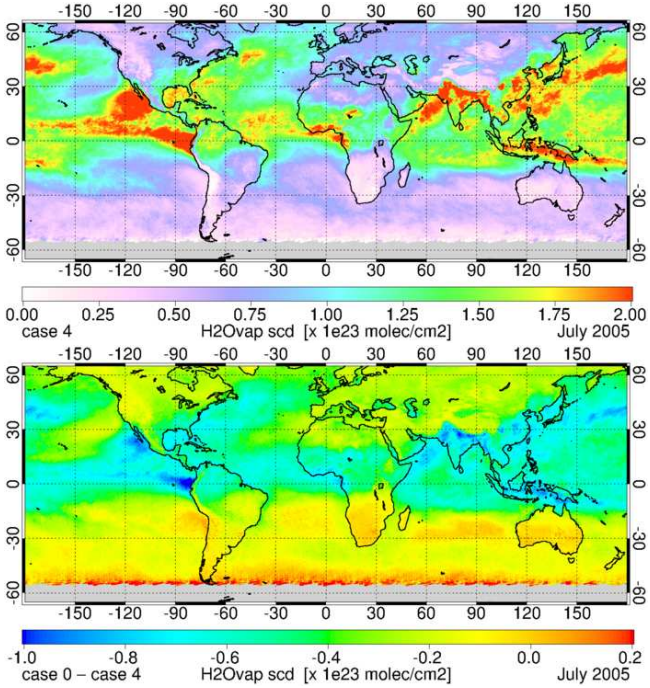

Fig. S17. Monthly average gridded updated (case 4; top panel) H_2O_{vap} slant column data for July 2005 and the corresponding difference with the current (case 0) data (lower panel).

sky UV-visible observations: validation of the technique through correlative comparisons, Atmos. Chem. Phys., 4, 2091-2106, doi:10.5194/acp-4-2091-2004, 2004.

Hendrick, F., Mahieu, E., Bodeker, G.E., Boersma, K.F., Chipperfield, M.P., De Mazière, M., De Smedt, I., Demoulin, P., Fayt, C., Hermans, C., Kreher, K., Lejeune, B., Pinardi, G., Servais, C., Stübi, R., van der A, R., Vernier, J.-P. and Van Roozendael, M.: Analysis of stratospheric NO_2 trends above Jungfraujoch using ground-based UV-visible, FTIR, and satellite nadir observations, Atmos. Chem. Phys., 12, 8851-8864, doi:10.5194/acp-12-8851-2012, 2012.

Hermans, C., Vandaele, A.C., Carleer, M., Fally, S., Colin, R., Jenouvrier, A., Coquart B. and Mérienne, M.-F.: Absorption cross-sections of atmospheric constituents: NO_2, O_2, and H_2O, Environ. Sci. & Pollut. Res., 6, 151-158, 1999.

Lambert, J.-C., Granville, J., Van Roozendael, M., Sarkissian, A., Goutail, F., Müller, J.-F., Pommereau, J.-P. and Russell III, J. M.: A climatology of NO_2 profile for improved Air Mass Factors for ground-based vertical column measurements, in: Stratospheric Ozone 1999, N.R.P. Harris, M. Guirlet and G.T. Amanatidis (Eds.), Air Pollution Research Report 73 (CEC DG XII), 703-706, 1999.

Lambert, J.-C., Granville, J., Van Roozendael, M., Müller,J.-F., Goutail, F., Pommereau, J.-P., Sarkissian, A., Johnston, P. V. and Russell III, J. M.: Global behaviour of atmospheric NO_2 as derived from the integrated use of satellite, ground-based network and balloon observations, in: Atmospheric Ozone - 19th Quad. Ozone Symp., Sapporo, Japan, 2000, Ed. by NASDA, 201-202, 2000.

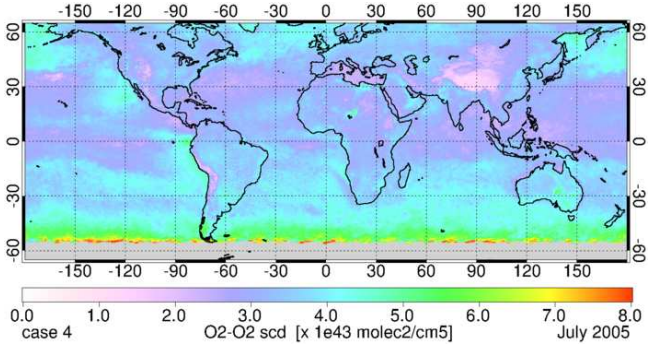

Fig. S18. Monthly average gridded O_2–O_2 slant column data for July 2005.

Lerot, C., Stavrakou, T., De Smedt, I., Müller, J.-F. and Van Roozendael, M.: Glyoxal vertical columns from GOME-2 backscattered light measurements and comparisons with a global model, Atmos. Chem. Phys., 10, 12059-12072, doi:10.5194/acp-10-12059-2010, 2010.

Platt, U., Marquard, L., Wagner, T. and Perner, D.: Corrections for zenith scatterd light DOAS, Geophys. Res. Lett., 24, 1759-1762, 1997.

Pommereau, J.-P. and Goutail, F.: O_3 and NO_2 ground-based measurements by visible spectrometry during arctic winter and spring 1988, Geophys. Res. Lett., 15, 891-894, 1988.

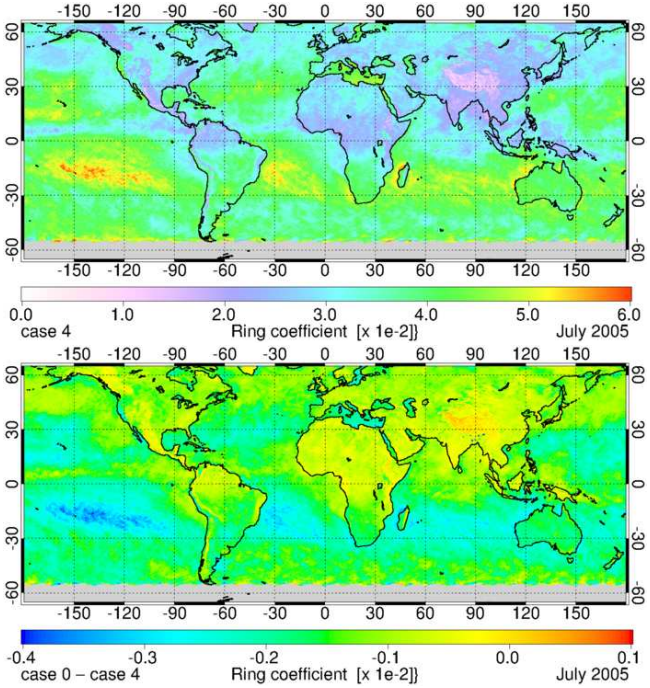

Fig. S19. Monthly average gridded updated (case 4; top panel) Ring coefficient data for July 2005 and the corresponding difference with the current (case 0) data (lower panel). The correction for the Ring coefficient of rows 0 and 59 from Sect. S4.3 was applied when gridding the data.

Pope, R.M. and Fry, E.S.: Absorption spectrum (380-700 nm) of pure water. II. Integrating cavity measurements, Appl. Optics, 36, 33, 8710-8723, doi:10.1364/AO.36.008710, 1997.

Richter, A., Begoin, M., Hilboll, A. and Burrows, J.P.: An improved NO_2 retrieval for the GOME-2 satellite instrument, Atmos. Meas. Tech., 4, 1147-1159, doi:10.5194/amt-4-1147-2011, 2011.

Rinsland, C.P., Jones, N.B., Connor, B.J., Logan, J.A., Pougatchev, N.S., Goldman, A., Murcray, F.J., Stephen, T.M., Pine, A.S., Zander, R., Mahieu, E. and Demoulin P.: Northern and southern hemisphere ground-based measurements of tropospheric carbon monoxide and ethane, J. Geophys. Res. 103, 28,197-28,217, doi:10.1029/98JD02515, 1998.

Rinsland, C.P., Weisenstein, D.K., Ko, M.K.W., Scott, C.J., Chiou, L.S., Mahieu, E., Zander, R. and Demoulin, P.: Post Mount Pinatubo eruption ground-based stratospheric column measurements of HNO_3, NO, and NO_2 and their comparison with model calculation, J. Geophys. Res., 108(D15), 4437, 11 pp., doi:10.1029/2002JD002965, 2003.

Roscoe, H.K., Van Roozendael, M., Fayt, C., du Piesanie, A., Abuhassan, N., Adams, C., Akrami, M., Cede, A., Chong, J., Clémer, K., Friess, U., Gil Ojeda, M., Goutail, F., Graves, R., Griesfeller, A., Grossmann, K., Hemerijckx, G., Hendrick, F., Herman, J., Hermans, C., Irie, H., Johnston, P.V., Kanaya, Y., Kreher, K., Leigh, R., Merlaud, A., Mount, G.H., Navarro, M., Oetjen, H., Pazmino, A., Perez-Camacho, M., Peters, E., Pinardi, G., Puentedura, O., Richter, A., Schönhardt, A., Shaiganfar, R., Spinei, E., Strong, K., Takashima, H., Vlemmix, T., Vrekoussis, M., Wagner, T., Wittrock, F., Yela, M., Yilmaz, S., Boersma, F., Hains, J., Kroon, M., Piters, A. and Kim, Y.J.: Intercomparison of slant column measurements of NO_2 and O_4 by MAX-DOAS and zenith-sky UV and visible spectrometers, Atmos. Meas. Tech., 3, 1629-1646, doi:10.5194/amt-3-1629-2010, 2010.

Rothman, L.S., Gordon, I.E., Babikov, Y., Barbe, A., Chris Benner, D., Bernath, P.F., Birk, M., Bizzocchi, L., Boudon, V., Brown, L.R., Campargue, A., Chance, K., Cohen, E.A., Coudert, L.H., Devi, V.M., Drouin, B.J., Fayt, A., Flaud, J.-M., Gamache, R.R., Harrison, J.J., Hartmann, J.-M., Hill C., Hodges, J.T., Jacquemart, D., Jolly, A., Lamouroux, J., Le Roy, R.J.,Li, G., Long, D.A., Lyulin, O.M., Mackie, C.J., Massie, S.T., Mikhailenko, S., Müller, H.S.P., Naumenko, O.V., Nikitin, A.V., Orphal, J., Perevalov, V., Perrin, A., Polovtseva, E.R., Richard, C., Smith, M.A.H., Starikova, E., Sung, K., Tashkun, S., Tennyson, J., Toon, G.C., Tyuterev, Vl.G. and Wagn, G.: The HITRAN 2012 molecular spectroscopic database, J. Quant. Spectrosc. Radiat. Transfer, 130, 4-50, doi:10.1016/j.jqsrt.2013.07.002, 2013.

Sneep, M., Sanders, A., de Haan, J. and Veefkind, P.: S5P/TROPOMI Static input for Level 2 processors, KNMI report S5P-KNMI-L2CO-0004-SD, issue 1.0.0, 2013.

Thalman, R. and Volkamer, R.: Temperature dependant absorption cross-sections of O_2–O_2 collision pairs between 340 and 630 nm at atmospherically relevant pressure Phys. Chem. Chem. Phys., 15, 15371-15381, doi:10.1039/C3CP50968K, 2013.

Van Roozendael, M., De Mazière, M. and Simon, P.C.: Ground-based visible measurements at the Jungfraujoch station since 1990, J. Quant. Spectrosc. Radiat. Transfer, 52, 231-240, 1994.

Vandaele A.C., Hermans, C., Simon, P.C., Carleer, M., Colin, R., Fally, S., Mérienne, M.F., Jenouvrier, A. and Coquart, B.: Measurements of the NO_2 absorption cross-section from 42000 cm-1 to 10000 cm-1 (238-1000 nm) at 220 K and 294 K, J. Quant. Spectrosc. Radiat. Transfer, 59, 171-184, 1998.

Vandaele, A. C., Fayt, C., Hendrick, F., Hermans, C., Humbled, F., Van Roozendael, M., Gil, M., Navarro, M., Puentedura, O., Yela, M., Braathen, G., Stebel, K., Tørnkvist, K., Johnston, P., Kreher, K., Goutail, F., Mieville, A., Pommereau, J.-P., Khaikine, S., Richter, A., Oetjen, H., Wittrock, F., Bugarski, S., Frieß, U., Pfeilsticker, K., Sinreich, R., Wagner, T., Corlett, G. and Leigh, R.: An intercomparison campaign of ground-based UV-Visible measurements of NO_2, BrO, and OClO slant columns. Methods of analysis and results for NO_2, J. Geophys. Res., 110, D08305, doi:10.1029/2004JD005423, 26 pp., 2005.

Voors, R., Dirksen, R., Dobber, M. and Levelt, P.: OMI in-flight wavelength calibration and the solar reference spectrum, in: Proceedings of the First Converence on Atmospheric Science, 8-12 May 2006, Frascati, Italy, ESA publication SP-628, 6 pp., 2006.

World Meteorological Organisation: WMO Anual Repport, Bass & Johnsten, 1975.

Zander, R., Mahieu, E., Demoulin, P., Duchatelet, P., Roland, G., Servais, C., De Mazière, M., Reimann, S. and Rinsland, C. P.: Our changing atmosphere: Evidence based on long-term infrared solar observations at the Jungfraujoch since 1950, Science of the Total Environment, 391/2-3, 185-195, 2008.